Electrical conductivity of SiO_2 at extreme conditions and planetary dynamos

Roberto Scipioni[a], **Lars Stixrude**[a,1], **and Michael P. Desjarlais**[b]

[a]Department of Earth Sciences, University College London, Gower Street, London WC1E 6BT, United Kingdom; [b]Pulsed Power Sciences Center, Sandia National Laboratory, Albuquerque, New Mexico 87185, USA

This manuscript was compiled on June 26, 2017

Ab intio molecular dynamics simulations show that the electrical conductivity of liquid SiO_2 is semi-metallic at the conditions of the deep molten mantle of the early Earth and super-Earths, raising the possibility of silicate dynamos in these bodies. Whereas the electrical conductivity increases uniformly with increasing temperature, it depends non-monotonically on compression. At very high pressure, the electrical conductivity decreases on compression, opposite to the behavior of many materials. We show that this behavior is caused by a novel compression mechanism: the development of broken charge ordering, and its influence on the electronic band gap.

density functional theory | ab initio molecular dynamics simulation | silica liquid | electrical conductivity | magma ocean | super-Earth | exoplanet

Planetary magnetic fields are produced by a dynamo process via fluid motions in a large rotating body of electrically conducting fluid within the planet's interior. In the present day Earth, the liquid portion of the iron-rich core produces the magnetic field. Early in Earth's history and before the inner core began to grow, the core may not have been able to cool sufficiently rapidly to sustain a dynamo (1). However, the rock record contains evidence for an ancient field of similar intensity to today's field within the first few 100 million years of Earth's history (2). What caused this early magnetic field is still unknown.

The Earth is thought to have been largely or completely molten early in its history (3). While the shallow portions of the magma ocean cooled quickly (4), a basal magma ocean, separated from the surface by a crystallizing layer, may have survived for a billion years or more (5). Could the basal magma ocean have produced a magnetic field? While a variety of different materials produce planetary magnetic fields, including iron, hydrogen, and ice, silicate dynamos are so far unknown (6).

A key uncertainty is the electrical conductivity σ of silicate liquid at the pressure-temperature conditions of the basal magma ocean (100 GPa, 5000 K). The conductivity must be sufficiently high for the dynamo process to operate. Recent models indicate that $\sigma > 10^3 - 10^4$ S m^{-1} is required (7). The possibility of silicate dynamos is not only relevant to the early Earth. Silicates appear to be the primary constituents of many super-Earth exoplanets. These planets may have hotter interiors that cool more slowly than Earth and may contain larger and longer lived basal magma oceans, so that Super-Earths may also have silicate dynamos. The conditions at the base of a 10 Earth mass Super-Earth mantle are expected to be 1000 GPa and 13,000 K (8).

Near ambient pressure, the electrical conductivity of silicate liquids is far too small to support dynamo activity and the dominant charge carriers are ions (9). However, experimental evidence suggests that the electrical conductivity of silicate liquids may be much greater at high pressure and temperature and that the dominant charge carriers may be electrons. Oxide liquids are found to become optically reflective along the Hugoniot at pressures of several hundred GPa (10–12). The electrical conductivity is not measured in shock wave studies, but inferred from the optical reflectivity via a Drude model. Previous theoretical calculations have relied on approximations to the exchange-correlation functional which are known to underestimate the electronic band gap (13, 14), leaving open the question of whether these simulations substantially overestimated σ.

Existing studies leave unclear the mechanism by which silicate liquids become reflective at high pressure. It is known from experiment and theory that the pressure-induced change of the structure of silicate liquids can be characterized by an increase in the Si-O coordination number from 4 near ambient pressure towards 9 at high pressure (15–17). A recent theoretical study argued that increased coordination was responsible for enhanced electrical conductivity at high pressure (14). However, the connection between coordination change and conductivity is not apparent. It has been suggested that the changes in silicate liquid structure on compression can be characterized by dissociation which, by analogy with that seen in hydrogen and oxygen, might explain closure of the electronic band gap (10, 13). However, hydrogen and oxygen are molecular rather than ionic systems and it is not clear the extent to which the analogy is suitable.

Here, we find that the electronic conductivity of liquid SiO_2 is sufficiently large to support a silicate dynamo, based on a more accurate approximation to the exchange-correlation functional than used in previous studies (HSE06) (18). Our

DRAFT

Significance Statement

We find that Earth's earliest magnetic field may have been produced in a deep magma ocean, and that silicate dynamos may exist in super-Earth exoplanets as well. Ab initio molecular dynamics simulations show that silicate liquids are semi-metallic at the extreme pressure and temperature conditions characteristic of planetary interiors. The electrical conductivity shows a remarkable non-monotonic dependence on pressure that reveals connections to the underlying atomic structure, and highlights broken charge ordering as a novel compression mechanism.

The authors declare no conflict of interest.

R.S. and L.S. designed and performed research, and analyzed data. M.P.D. contributed new tools. R.S., L.S., and M.P.D. wrote the paper.

[1] To whom correspondence should be addressed. E-mail: l.stixrudeucl.ac.uk

Fig. 1. Ab initio electrical conductivity computed with PBEsol (full lines and closed symbols) and with HSE06 (open symbols). We also compare with the Mott-Ziman theoy (dashed lines, see text) and the minimum metallic conductivity of Mott (19) (grey band) .

Fig. 2. Electronic density of states at 50,000 K (top) and 10,000 K (bottom) over the density range explored compared with the free-electron density of states at ρ=3.67 g cm^{-3} (black dashed line), and the contribution of the oxygen p band at the same density (dashed green line).

results further show a remarkable non-monotonic dependence of the electrical conductivity on compression. This behavior is crucial for revealing the connection between structural change and electronic and thermodynamic properties at high pressure. We show that a new mode of high-pressure structural change: broken charge ordering, is responsible for the variation of electrical conductivity with density and temperature.

Our first principles molecular dynamics simulations show that at high temperature ($T \geq$ 20,000 K) the electrical conductivity increases monotonically with compression, reaching half the minimum metallic value at the highest pressure-temperature conditions explored (Fig. 1). For example, at 50,000 K, the conductivity increases by a factor of 3 from ρ=2.2 to ρ=7.33 g cm^{-3} where σ=4 × 10^5 S m^{-1}. The electrical conductivity increases with increasing temperature at all densities, for example, by a factor of 30 between 4000 K and 50,000 K at ρ=3.67 g cm^{-3}.

At lower temperature ($T \leq 10{,}000$ K), the conductivity displays a maximum value at intermediate compression (Fig. 1). The conductivity increases with compression from ρ=2.2 to ρ=3.67 g cm^{-3} and then decreases on further compression, by a factor of ten from ρ=3.67 to $\rho = 7.33$ g cm^{-3} at 6000 K. The tendency for the conductivity to decrease with compression at very high pressure was also noted in a previous study (14), although that study did not explore the pressure-temperature range necessary to reveal the extremum that we find. The electrical conductivity computed with the HSE06 functional is lower than that computed with PBEsol, as expected, although the difference is not large (< 25 % (Fig. 1)).

To understand our results, we have examined the electronic structure (Fig. 2 and Supplementary Information). At high temperature, the electronic density of states is nearly free-electron like. There is no gap and the density of states at the Fermi level is within 5 % of the free electron value. As the valence electrons are only weakly bound we expect the Ziman theory (20) to yield a reasonable approximation to the conductivity. As expected, the Ziman formula reproduces our first principles results for the electrical conductivity to within 30 % at $T \geq$ 20,000 K (Fig. S4). It fails, however, at lower temperature: the Ziman theory cannot capture the local maximum in σ that appears near ρ=3.67 g cm^{-3} for $T \leq$ 10,000 K.

The Ziman formula fails at lower temperature because the electronic structure is no longer free-electron like (Fig. 2). A prominent pseudo-gap appears in the electronic density of states, which deepens on compression. The appearance of a pseudo-gap on cooling, which is in excellent agreement with experimental XANES spectra (21), has a profound effect on the electrical conductivity. To see this, we recall that the conductivity diminishes with the density of states at the Fermi level. In the Mott-Ziman theory (22, 23)

$$\sigma_{MZ} = g^2 \sigma_Z \tag{1}$$

where σ_Z is the Ziman result and

$$g = \frac{\bar{N}(\mu)}{N_{Free}(E_F)} \tag{2}$$

is the ratio of the temperature-smoothed density of states at the chemical potential $\bar{N}(\mu)$ to that of the free electron system N_{Free}. At 10,000 K, the value of g^2 diminishes from 0.64 at $\rho = 3.67$ g cm^{-3} to 0.22 at $\rho = 7.33$ g cm^{-3} accounting for the drop in conductivity over this density range. The good agreement between our results and the Mott-Ziman theory (to within 30 % at all conditions, Fig. 1) shows that the pressure-induced decrease in the conductivity at high pressure and low temperature is caused by the decrease in g as the pseudo-gap deepens on compression.

Fig. 3. Structure factors at ρ=7.33 g cm^{-3} (top) and T=10,000 K (bottom).

Fig. 4. Radial distribution function of SiO$_2$ (green) compared with that of isoelectronic Ne (black) at 10,000 K. The inset shows the comparison at ρ=7.33 g cm^{-3} and 50,000 K (SiO$_2$: red, Ne: black). Schematics illustrate (top) charge ordering characteristic of silicate liquids, consisting of alternating neighbor shells of cations (blue) and anions (red), and (bottom) the broken charge ordered structure characteristic of extreme pressure in which the nearest neighbor shell contains like as well as unlike charged ions.

Fig. 5. Isochoric heat capacity (top) and reflectivity at 532 nm (bottom) for SiO$_2$ along the fused silica (red) and quartz (blue) Hugoniots. Lines are our results, while experimental data are shown as open circles (10) and squares (26). The black circles indicate the heat capacity computed via finite difference between the two Hugoniots. In the lower figure the colored bands indicate the sensitivity to the exchange-correlation functional comparing PBEsol results (upper lines) with those of HSE06 (lower lines).

It remains to relate the appearance of the pseudogap to the structure of the liquid. For liquids, in the nearly free electron limit, the pseudogap appears because of scattering of electronic states from density fluctuations in the liquid as measured by the structure factor, $S(q)$ (24, 25). The amplitude of the first peak in the structure factor varies considerably on compression and cooling (Fig. 3). The depth of the pseudogap δ increases linearly with the amplitude of the first peak in the structure factor $S(q_P)$ as $\delta \approx 2[S(q_P) - 1]|w(q_P)|$, where $w(q)$ is the effective electron-ion interaction (25). For example, at 10,000 K, $S(q_P) - 1$ increases four-fold from ρ=3.67 to ρ=7.33 g cm^{-3}, in reasonable accord with the three-fold decrease in the the density of states at the Fermi level over the same range of compression. We see a similar pattern on cooling: as $S(q_P)$ grows (Fig. 3), the pseudogap deepens and the electrical conductivity diminishes.

Our simulations highlight a novel mode of compression in silicate liquids that accounts for the growth of the first peak in the structure factor on compression (Fig. 4). At low pressure, it is well known that silicate liquid structure is dominated by charge-ordering as is typical of ionically bonded systems: cations are surrounded by a first neighbor shell of anions and vice versa, producing well separated peaks for Si-O and O-O correlations. For example, in SiO$_2$ liquid at low pressure, the O-O distance (2.6 Å) is much larger than the Si-O distance (1.6 Å) (27). At very high pressure, we find that

DRAFT

charge-ordering breaks down. Like charges begin to appear in the first coordination shell, Si-O and O-O peaks overlap and the liquid structure approaches that of isoelectronic neon (Fig. 4). This peak overlap accounts for the large increase in the amplitude of the first peak in the structure factor as density increases from ρ=3.67 to ρ=7.33 g cm^{-3} (Fig. 3).

Broken charge ordering is also important in high pressure silicate crystal structures. The novel high pressure structure of (28) shows remarkably high 10-fold Si-O coordination. Using the reported atomic coordinates and lattice parameters we have analyzed the predicted structure and found another remarkable feature: the smallest O-O distance (1.754 Å) is less than the smallest Si-O distance (1.790 Å). The crowding of O atoms at high pressure leads to more efficient packing as shorter-ranged repulsive forces begin to dominate over longer-ranged Coulombic forces. This behavior recalls predictions in simple ionic systems, such as CsI, where the structure approaches that of isoelectronic Xe at high pressure (29). In SiO_2 much higher pressures are required to break the charge ordering as compared with CsI, because the ionic bonding in SiO_2 is much stronger. Crowding and increased interaction among O atoms also influences the electronic structure by producing increased hybridization of the O valence states with conduction bands, dominating the electronic density of states in the vicinity of the pseudo-gap (Fig. 2).

Previous studies have interpreted the variation of the heat capacity along the Hugoniot to indicate dissociation of SiO_2 at large compressions, a pattern of structural change very different to what we have described. To examine this difference more closely, we have computed the heat capacity along the Hugoniot from our simulations. The ab initio heat capacity shows variations with temperature along the Hugoniot very similar to that found experimentally (Fig. 5). We interpret these variations as non-dissociative changes in atomic and electronic structure that are common to a wide variety of liquids.

At the highest temperatures ($T > 30{,}000$ K), the heat capacity increases on heating, reflecting the increase with temperature of the electronic contribution to the heat capacity, C_V^{el}. The increase of C_V^{el} on heating reflects the growing density of states at the Fermi level with increasing temperature (Fig. 2), behavior that is seen in many silicate liquids (30). At intermediate temperature (10,000 K $< T <$ 30,000 K), the heat capacity decreases with increasing temperature. At these conditions, the non-electronic contribution to the heat capacity C_V^{ion} dominates. This behavior is seen in a wide variety of liquids, including simple, non-bonded liquids interacting through hard sphere or soft-sphere potentials. Fundamental measure theory (31) predicts $C_V \propto T^{-2/5}$ in approximate accord with our results for silica liquid. We have previously found that a variety of silicate liquids closely follow this relation over a wide range of temperature (30). The heat capacity is everywhere much larger than the Dulong-Petit value, reflecting structural degrees of freedom in the liquid that are unavailable to solids. Indeed, previous studies have shown that the structure of silicate liquids changes substantially on isochoric heating. For example, in SiO_2 liquid at low pressure, the liquid structure, characterized by almost perfect 4-fold Si-O coordination at the lowest temperatures, shows increasing numbers of 5- and 3-coordinated Si on isochoric heating (27). The rate of structural change initially increases on heating, and then saturates, producing a local maximum in the heat capacity (32).

Our first principles predictions of the optical reflectivity agree well with experimental measurements although experimental uncertainties are significant (Fig. 5). We find that HSE06 predicts smaller values of the reflectivity in better agreement with experiment as compared with PBEsol . The smaller value of the HSE06 reflectivity is expected: HSE06 predicts band gaps in crystalline polymorphs of SiO_2 that are in excellent agreement with experiment and much larger than those predicted by PBEsol ($\sim$ 50 %), apparently overcoming the well known tendency of many functionals to seriously underpredict the band gap (33). In this context, the difference between our HSE06 and PBEsol results is perhaps surprisingly small, amounting to less than 0.02. However, it is important to remember that while different functionals are often compared in terms of the predicted band gap, our system has no gap, and arguments based on the behavior of functionals in wide gap systems may not apply to the liquid. We believe that the absence of a gap in our system mutes the effects of exact exchange, reducing the difference between HSE06 and PBEsol. We have not considered explicit temperature dependence of the exchange-correlation functional in our calculations as a recent investigation shows these effects to be small, amounting to 10 % in the value of σ (34).

Our results indicate that the magnetic field in the early Earth could have been generated by a silicate dynamo. From our results (Fig. 1), we find an interpolated value of the electrical conductivity $\sigma = 5700$ S m^{-1} at 100 GPa and 5000 K. For a 10 Earth mass super Earth, we find an even higher value: $\sigma = 125,500$ S m^{-1} at 1000 GPa and 13,000 K. While these values of σ are sub-metallic, they exceed the minimum value required in magma ocean dynamo models (7) and those of planetary dynamos in our solar system: the conductivity of the dynamo generating regions of Neptune and Uranus is thought to be 2000 S m^{-1} (35). Our predicted values for pure silica may underestimate the conductivity of the magma ocean: additional components, particularly FeO and CaO may increase the conductivity. Further, it is known that MgO and $MgSiO_3$ become optically reflective along the Hugoniot at conditions similar to those at the base of a super-Earth magma ocean (11, 36). We look forward to a broader class of magnetohydrodynamic simulations of the ancient field to include the possibility of an early silicate dynamo. The analysis of our results in terms of the Mott-Ziman theory provides a framework for understanding optical, electrical, and thermodynamic properties in these systems, as well as other liquids that may be accessibe to experimental investigation at extreme conditions.

Materials and Methods

Our molecular dynamics simulations are based on density functional theory in the PBEsol (37) approximation, using the projector augmented wave (PAW) method (38), as implemented in the VASP code (39). Born-Oppenheimer simulations are performed in the canonical ensemble using the Nosé-Hoover thermostat with 96 atoms and run for 10-15 ps with 1 fs time step. We assume thermal equilibrium between ions and electrons via the Mermin functional (40). Sampling the Brillouin zone at the Gamma point and a basis-set energy cutoff of 500 eV were found to be sufficient to converge energy and pressure to within within 2 meV/atom and 0.2 GPa, respectively. For comparison, we also performed ab initio simulations of neon with the same settings. In addition to standard thermodynamic

DRAFT

quantities, we also compute the isochoric heat capacity

$$C_V(V,T) = C_V^{\mathrm{ion}}(V,T) + C_V^{\mathrm{el}}(V,T) \quad [3]$$

with the ionic contribution given by the fluctuation formula (41)

$$C_V^{\mathrm{ion}} = \frac{\langle \Delta E \rangle^2}{k_B T^2} \quad [4]$$

where $\langle \Delta E \rangle^2$ is the mean squared fluctuation in the internal energy, and the electronic contribution C_V^{el} by an accurate fit to the electronic entropy versus temperature using a generalization of the functional form used in our previous studies (30) (Fig. S6 and Supporting Information).

We compute the electrical conductivity via the Kubo-Greenwood formula (42) and the dielectric constant using the Random Phase Approximation (43) as implemented in VASP from a series of at least 10 uncorrelated snapshots at each volume-temperature condition. We perform dielectric constant calculations in both PBEsol and HSE06 (18). We found that a 3x3x3 k-point mesh and 2000 electronic bands were sufficient to yield converged results. We also compared with the results of a larger system (144 atoms) and found no significant differences to electronic density of states, electrical conductivity, or dielectric constant. We compute the electronic density of states (DOS) by averaging over at least 20 snapshots well separated in time from the MD trajectories. We sample the Brillouin zone on a $3 \times 3 \times 3$ mesh, and use the Fermi-Dirac distribution with temperature equal to the ionic temperature to smooth the DOS.

ACKNOWLEDGMENTS. Research supported by the European Research Council under Advanced Grant No. 291432 MoltenEarth (FP7/2007-2013). Calculations were performed on the Iridis computing cluster partly owned by University College London, and ARCHER of the UK national high-performance computing service. We thank Dylan Spaulding for providing data; Dylan Spaulding, Simon Hunt, and Paul McMillan for valuable discussions, and Dario Alfé and Eero Holmström for comments on the manuscript. Sandia National Laboratories is a multi-mission laboratory managed and operated by National Technology and Engineering Solutions of Sandia, LLC., a wholly owned subsidiary of Honeywell International, Inc., for the U.S. Department of Energy's National Nuclear Security Administration under Contract No. DE-NA0003525.

1. Labrosse S (2015) Thermal evolution of the core with a high thermal conductivity. *Physics of the Earth and Planetary Interiors* 247:36–55.
2. Tarduno JA, Cottrell RD, Davis WJ, Nimmo F, Bono RK (2015) A hadean to paleoarchean geodynamo recorded by single zircon crystals. *Science* 349(6247):521–524.
3. Nakajima M, Stevenson DJ (2015) Melting and mixing states of the earth's mantle after the moon-forming impact. *Earth and Planetary Science Letters* 427:286–295.
4. Karki BB, Stixrude LP (2010) Viscosity of $MgSiO_3$ liquid at earth's mantle conditions: Implications for an early magma ocean. *Science* 328(5979):740–742.
5. Labrosse S, Hernlund JW, Coltice N (2007) A crystallizing dense magma ocean at the base of the earth's mantle. *Nature* 450(7171):866–869.
6. Stanley S, Glatzmaier GA (2010) Dynamo models for planets other than earth. *Space Science Reviews* 152(1-4):617–649.
7. Ziegler LB, Stegman DR (2013) Implications of a long-lived basal magma ocean in generating earth's ancient magnetic field. *Geochemistry Geophysics Geosystems* 14(11):4735–4742.
8. Stixrude L (2014) Melting in super-earths. *Philosophical Transactions of the Royal Society a-Mathematical Physical and Engineering Sciences* 372(2014):20130076.
9. Gaillard F (2004) Laboratory measurements of electrical conductivity of hydrous and dry silicic melts under pressure. *Earth and Planetary Science Letters* 218(1-2):215–228.
10. Hicks DG, et al. (2006) Dissociation of liquid silica at high pressures and temperatures. *Physical Review Letters* 97(2):025502.
11. Spaulding DK, et al. (2012) Evidence for a phase transition in silicate melt at extreme pressure and temperature conditions. *Physical Review Letters* 108(6):065701.
12. McWilliams RS, et al. (2012) Phase transformations and metallization of magnesium oxide at high pressure and temperature. *Science* 338(6112):1330–1333.
13. Laudernet Y, Clerouin J, Mazevet S (2004) Ab initio simulations of the electrical and optical properties of shock-compressed SiO_2. *Physical Review B* 70(16):165108.
14. Mazevet S, Tsuchiya T, Taniuchi T, Benuzzi-Mounaix A, Guyot F (2015) Melting and metallization of silica in the cores of gas giants, ice giants, and super earths. *Physical Review B* 92(1):014105.
15. Stixrude L, Karki B (2005) Structure and freezing of $MgSiO_3$ liquid in earth's lower mantle. *Science* 310(5746):297–299.
16. Sanloup C, et al. (2013) Structural change in molten basalt at deep mantle conditions. *Nature* 503(7474):104–107.
17. Denoeud A, et al. (2016) High-pressure structural changes in liquid silica. *Physical Review E* 94(3):031201(R).
18. Heyd J, Scuseria GE, Ernzerhof M (2006) Hybrid functionals based on a screened coulomb potential (vol 118, pg 8207, 2003). *Journal of Chemical Physics* 124(21):219906.
19. Mott NF (1972) Conduction In non-crystalline systems .9. minimum metallic conductivity. *Philosophical Magazine* 26(4):1015–1026.
20. Ziman JM (1961) A theory Of the electrical properties Of liquid metals - the monovalent metals. *Philosophical Magazine* 6(68):1013–1034.
21. Denoeud A, Benuzzi-Mounaix A, et al. AR (2014) Metallization of warm dense SiO_2 studied by XANES spectroscopy. *Physical Review Letters* 113(11):116404.
22. Mott NF, Davis EA (1979) *Electronic Processes in Non-cyrstalline Materials.* (Oxford University Press, Oxford), 2 edition.
23. Stixrude L, Jeanloz R (2008) Fluid helium at conditions of giant planetary interiors. *Proceedings Of The National Academy Of Sciences Of The United States Of America* 105:11071–11075.
24. Nagel SR, Tauc J (1975) Nearly-free-electron approach To theory Of metallic glass alloys. *Physical Review Letters* 35(6):380–383.
25. Jank W, Hafner J (1990) Structural and electronic-properties Of the liquid polyvalent elements .2. the divalent elements. *Physical Review B* 42(11):6926–6938.
26. Spaulding DK (2010) Ph.D. thesis (University of California at Berkeley).
27. Karki BB, Bhattarai D, Stixrude L (2007) First-principles simulations of liquid silica: Structural and dynamical behavior at high pressure. *Physical Review B* 76(10):104205.
28. Lyle MJ, Pickard CJ, Needs RJ (2015) Prediction of 10-fold coordinated TiO_2 and SiO_2 structures at multimegabar pressures. *Proceedings of the National Academy of Sciences of the United States of America* 112(22):6898–6901.
29. Ross M, Rogers FJ (1985) Structure of dense shock-melted alkali-halides - evidence for a continuous pressure-induced structural transition in the melt. *Physical Review B* 31(3):1463–1468.
30. de Koker N, Stixrude L (2009) Self-consistent thermodynamic description of silicate liquids, with application to shock melting of MgO periclase and $MgSiO_3$ perovskite. *Geophysical Journal International* 178(1):162–179.
31. Rosenfeld Y, Tarazona P (1998) Density functional theory and the asymptotic high density expansion of the free energy of classical solids and fluids. *Molecular Physics* 95(2):141–150.
32. Hujo W, Jabes BS, Rana VK, Chakravarty C, Molinero V (2011) The rise and fall of anomalies in tetrahedral liquids. *Journal of Statistical Physics* 145(2):293–312.
33. Xiao B, et al. (2013) Testing density functionals for structural phase transitions of solids under pressure: Si, SiO_2, and Zr. *Physical Review B* 88(18):184103.
34. Karasiev VV, Calderin L, Trickey SB (2016) Importance of finite-temperature exchange correlation for warm dense matter calculations. *Physical Review E* 93(6):063207.
35. Stanley S, Bloxham J (2006) Numerical dynamo models of uranus? and neptune?s magnetic fields. *Icarus* 184:556–572.
36. Cebulla D, Redmer R (2014) Ab initio simulations of MgO under extreme conditions. *Physical Review B* 89(13):134107.
37. Perdew JP, et al. (2008) Restoring the density-gradient expansion for exchange in solids and surfaces. *Physical Review Letters* 100(13):136406.
38. Kresse G, Joubert D (1999) From ultrasoft pseudopotentials to the projector augmented-wave method. *Physical Review B* 59(3):1758–1775.
39. Kresse G, Furthmuller J (1996) Efficient iterative schemes for ab initio total-energy calculations using a plane-wave basis set. *Physical Review B* 54(16):11169–11186.
40. Mermin ND (1965) Thermal properties of inhomogeneous electron gas. *Physical Review* 137(5A):A1441–A1443.
41. Allen MP, Tildesley DJ (1989) *Computer Simulation of Liquids.* (Clarendon Press, Oxford).
42. Desjarlais MP, Kress JD, Collins LA (2002) Electrical conductivity for warm, dense aluminum plasmas and liquids. *Physical Review E* 66(2):025401(R).
43. Gajdos M, Hummer K, Kresse G, Furthmuller J, Bechstedt F (2006) Linear optical properties in the projector-augmented wave methodology. *Physical Review B* 73(4):045112.
44. Pozzo M, Desjarlais MP, Alfe D (2011) Electrical and thermal conductivity of liquid sodium from first-principles calculations. *Physical Review B* 84(5):054203.
45. Ashcroft NW, Mermin ND (1976) *Solid state physics.* (Holt Rinehart and Winston, New York).
46. Ghosh G (1999) Dispersion-equation coefficients for the refractive index and birefringence of calcite and quartz crystals. *Optics Communications* 163(1-3):95–102.
47. Ashcroft NW, Langreth C (1967) Structure of binary liquid mixtures .2. resistivity of alloys and ion-ion interaction. *Physical Review* 159(3):500–510.
48. Wasserman E, Stixrude L, Cohen RE (1996) Thermal properties of iron at high pressures and temperatures. *Physical Review B* 53:8296–8309.

DRAFT

Supporting Information (SI)

Electronic DOS. We compute the electronic density of states by averaging over at least 20 uncorrelated snapshots from our MD trajectories (Fig. S1). We sample the Brillouin zone with k-point meshes up to $5 \times 5 \times 5$ k- points, although convergence is usually achieved for a $3 \times 3 \times 3$ mesh. We use the Fermi-Dirac distribution with temperature equal to the ionic temperature to smooth the DOS.

Ab initio Electrical Conductivity. For PBEsol calculations, we compute the static (DC) electrical conductivity from ab initio wavefunctions using the Kubo-Greenwood formalism as implemented in VASP (42) (Fig. S2). Assuming isotropy, the elements of the conductivty tensor satisfy the relations $\sigma_{\alpha\beta} = \sigma\delta_{\alpha\beta}$ where $\delta_{\alpha\beta}$ is the Kroenecker delta. The frequency dependent conductivity is

$$\sigma(\omega) = \frac{2\pi e^2\hbar^2}{3m^2\omega\Omega}\sum_{\vec{k}}\sum_{ij}[f(\epsilon_i,\vec{k}) - f(\epsilon_j,\vec{k})] \times |\langle\psi_{i,\vec{k}}|\nabla|\psi_{j,\vec{k}}\rangle|^2\delta(\epsilon_i - \epsilon_j - \hbar\omega) \quad [5]$$

where the sums are over the Brillouin zone and pairs of states, respectively, f is the Fermi occupation, ψ is the wavefunction, ϵ is the eigenvalue, ω is the frequency, and Ω is the volume of the simulation cell.

In our computations, the δ function is replaced by a Gaussian of width Δ given by the average spacing between eigenvalues weighted by the corresponding change in the Fermi function (44). As the behavior of Eq. 5 becomes unphysical for $\hbar\omega < \Delta$, we find the DC conductivity by linearly extrapolating to zero frequency.

Ab initio Optical Properties. We compute the complex dielectric constant ϵ via the random phase approximation (RPA) as implemented in VASP (43). The reflectivity is (45)

$$r(\omega) = \frac{[n_0(\omega) - n(\omega)]^2 + [k_0(\omega) - k(\omega)]^2}{[n_0(\omega) + n(\omega)]^2 + [k_0(\omega) + k(\omega)]^2} \quad [6]$$

where $n = \mathrm{Re}(\kappa)$, $k = \mathrm{Im}(\kappa)$, $\kappa = \sqrt{\epsilon}$ and subscript 0 indicates the values of the unshocked material. We use established values (46) $n_0(\omega_x) = 1.461$ for fused silica, and $n_0(\omega_x) = 1.546$ for quartz at ambient conditions and the frequency of the experimental probe ω_x=532 nm (2.33 eV); $k_0(\omega_x) = 0$ for both phases.

For HSE calculations, we compute the electrical conductivity from the dielectric constant (Fig. S2)

$$\sigma(\omega) = \omega\mathrm{Im}(\epsilon) \quad [7]$$

We have found that the frequency dependence of the conductivity can be represented by a Drude form plus a Lorentz peak

$$\sigma(\omega) = A\omega^2/((B - \omega^2)^2 - C\omega^2) + \sigma(0)/(1 + \omega^2\tau^2) \quad [8]$$

which then yields the DC conductivity $\sigma(0)$ as a parameter of the fit.

Structure Factor. Figure S3 shows our results for the total structure factor. In order to evaluate the suitability of the nearly free electron picture, we compare the form of the structure factor to that of the electronic density of states. In this limit, the gap appears at the energy $W \approx \hbar^2/(2m)(q_P/2)^2$ above the bottom of the valence band (24), where q_P is the position of the first peak in the structure factor. For example, at 7.33 g cm^{-3} and 10,000 K the first peak in the structure factor is located at $q_P = 4.3$ Å^{-1} (Fig. S3), yielding $W = 18$ eV, in reasonable agreement with the position of the pseudo-gap in our simulations (Fig. S1).

We further illustrate the structure of the liquid via the partial radial distribution functions (Fig. S4) and a snapshot from the simulation at 7.33 g cm^{-3} and 50,000 K (Fig. S5).

Mott-Ziman Formalism. The electrical conductivity in the Mott-Ziman theory is given by

$$\sigma_{MZ}^{-1} = \frac{a_0 h}{g^2 2e^2}\frac{k_{TF}^2}{64\pi Z E_F^2}\int_0^{2k_F} q^3 S(q)u(q)^2 dq \quad [9]$$

where $S(q)$ is the structure factor from our simulations, k_F and k_{TF} are the Fermi and Thomas-Fermi wave vectors, respectively, E_F is the Fermi energy, the conductivity quantum $2e^2/ha_0 = 1.464 \times 10^6$ S m^{-1} , and we have assumed an unscreened pseudopotential $u(q) = -4\pi Ze^2/q^2$ with $Z = 4$ for Si and for O. We note that, in general, for a binary system, the total structure factor must be replaced by (47)

$$S(q)u(q)^2 \rightarrow S_{22}(q)u_2(q)^2 + (1 - x)S_{11}(q)u_1(q)^2 + 2[x(1 - x)]^{1/2}S_{12}(q)u_1(q)u_2(q) \quad [10]$$

Where S_{ab} are the Ahscroft-Langreth partial structure factors, u_a is the pseudopotential of component a and x is the concentration of species 2. In our case the effective valences of both species are taken to be equal (Z=4) corresponding to Be and Ne cores for O and Si, respectively. Therefore the unscreened pseudopotentials $u_1 = u_2 = u$, and these terms can be factored out: the combined contribution of the partial structure factors is just the total structure factor and the right hand side of Eq. 10 reduces to $S(q)u^2(q)$.

Our Mott-Ziman results are shown as dashed lines in Fig. 1 of the main text. For comparison, we show our Ziman results ($g = 1$) in Fig. S6.

Hugoniot. We compute the ab initio Hugoniot (Fig. S7) from:

$$E(V,T) - E_0 = \frac{1}{2}[P(V,T) + P_0](V_0 - V) \quad [11]$$

where E_0, P_0, V_0 are the energy, pressure and volume of the initial unshocked state. We compute with VASP E_0 and V_0 at $P_0 = 0$ for initial unshocked states: quartz and fused silica. The latter is obtained by quenching our MD simulations at $\rho = 2.20$ g cm^{-3}. Solutions to Eq. 11 are found via interpolation of our MD results (48).

Heat Capacity. Under the assumption of thermal equilibrium between ions and electrons the total heat capacity

$$C_V(V,T) = C_V^{\mathrm{ion}}(V,T) + C_V^{\mathrm{el}}(V,T) \quad [12]$$

We compute the ionic contribution via the fluctuation formula (41)

$$C_V^{\mathrm{ion}} = \frac{\langle\Delta E\rangle^2}{k_B T^2} \quad [13]$$

where $\langle\Delta E\rangle^2$ is the mean squared fluctuation in the internal energy.

Our results for the electronic contribution to the heat capacity at all volumes and temperatures are summarized in Figure S8. We obtain the electronic contribution from the electronic entropy, which we have found is well represented by

$$S^{\mathrm{el}}(V,T) = \lambda(V)[\ln(T/T_0)]^2 \quad [14]$$

yielding

$$C_V^{\mathrm{el}} = \lambda(V)\ln(T/T_0) \quad [15]$$

In Figure S8 we show an example of the fit obtained. The functional form is a generalization of that used in our previous work over a more limited range of temperature (30).

In Figure S9 we show the temperature dependence of the total heat capacity C_V calculated at different volumes for liquid SiO$_2$. We find a local maximum at temperatures 6000 K $< T <$ 10,000 K for all volumes. At higher temperature, the electrical contribution dominates and the heat capacity increases monotonically on heating.

The method we have used for computing the heat capacity has the advantage that variations of C_V with temperature are more robustly recovered. The heat capacity may also be computed via finite difference

$$\bar{C_V}(\bar{T}) = \frac{E(T_2) - E(T_1)}{T_2 - T_1} \quad [16]$$

where the overbars indicate mean values. We demonstrate that our values of the heat capacity are consistent with values computed via Eq. 16 in Figure S9.

DRAFT

Fig. S1. Electronic DOS for different densities and temperatures. The continuous blue line is the free-electron DOS.

Fig. S2. Comparison of electrical conductivity computed from the Kubo-Greenwood method at ρ=7.33 g cm^{-3} and T=10,000 K (green), ρ=7.33 g cm^{-3} and T=20,000 K (orange), and ρ=3.67 g cm^{-3} and T=10,000 K (black). Also shown is the conductivity computed from the dielectric constant at ρ=7.33 g cm^{-3} and T=10,000 K in PBEsol (short dashed) and HSE06 (lond-dashed).

Fig. S3. Total structure factor for SiO$_2$ at different densities and temperatures. The dashed black lines indicate the upper limit of the Ziman integral $(2k_F)$.

Fig. S4. Total radial distribution function of SiO$_2$ (green) and the partial radial distribution functions O-Si (solid red), O-O (dashed red) Si-Si (small dashed red) at 10,000 K and the density indicated and (inset) at ρ=7.33 g cm^{-3} and 50,000 K.

Fig. S5. Snapshot from the simulation at ρ=7.33 g cm^{-3} and 50,000 K showing (blue) Si and (red) O atoms and distances nearer than 2.0 Å shown as bonds. We note that the choice of distance cutoff is somewhat arbitrary as the first coordination shell is not well defined at these conditions as is evident from the radial distribution function (Fig. S4). Our choice emphasizes the similar number of O-O to O-Si nearest nieghbors and thus the breakdown of charge ordering.

Fig. S6. Ab initio electrical conductivity computed with PBEsol (full lines and closed symbols) and with HSE06 (open symbols) compared with the Ziman formula ($g = 1$, dashed lines).

Fig. S7. Principle Hugoniots of fused silica (red) and quartz (blue) as computed from our first principles simulations (lines) and measured experimentally (symbols) (10).

Fig. S8. Electronic heat capacity as a function of temperature at various densities from our simulations. (Inset) Electronic entropy from our simulations at ρ=7.33 g cm^{-3} (symbols) and the fit to these results (Eq. 14).

Fig. S9. Total heat capacity as a function of temperature at various densities from our simulations. (Inset) Comparison of the total heat capacity computed with the fluctuation formula (Eq. 13) and the electronic entropy (Eqs. 15) at T=8000 K (blue) and T=10,000 K (red) to that computed via finite difference (Eq. 16) with T_1=8000 K and T_2=10,000 K (grey).

DRAFT

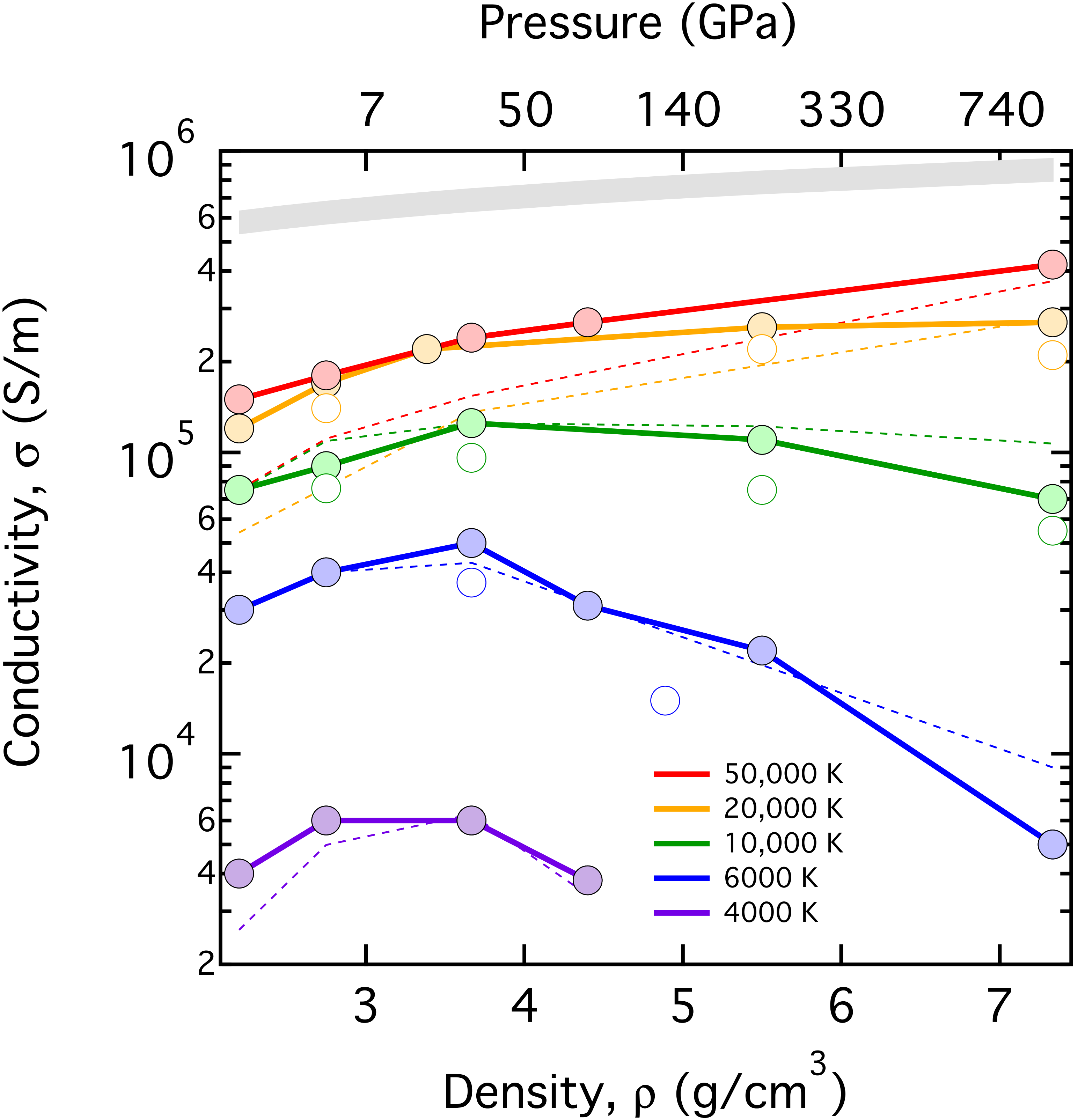
Pressure (GPa)
7
50
140
330
740
10^6
6
4
2
10^5
6
4
2
10^4
6
4
2
Conductivity, σ (S/m)
3
4
5
6
7
Density, ρ (g/cm^3)
50,000 K
20,000 K
10,000 K
6000 K
4000 K

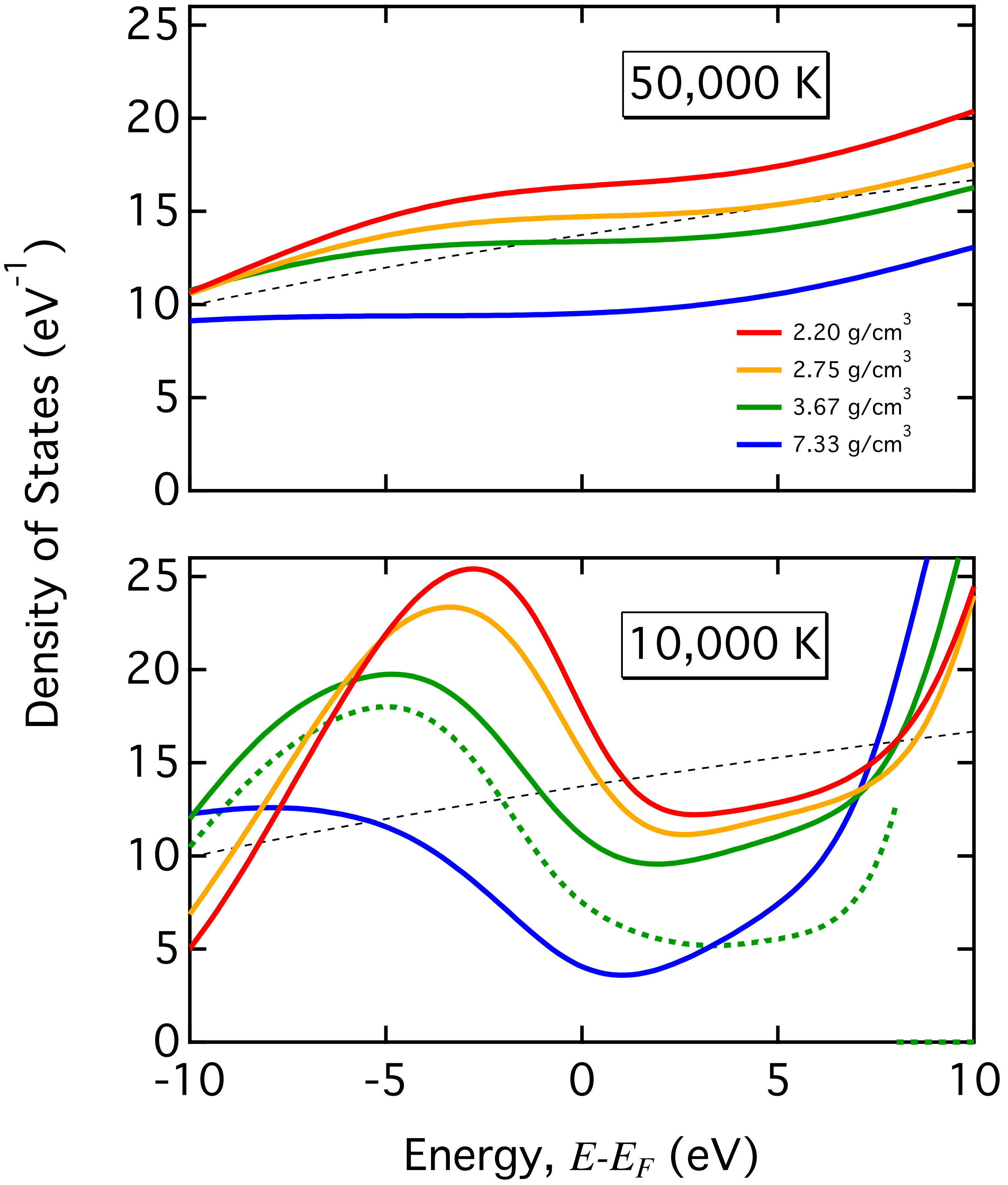
50,000 K
10,000 K
2.20 g/cm^3
2.75 g/cm^3
3.67 g/cm^3
7.33 g/cm^3
Density of States (eV^{-1})
Energy, E-E_F (eV)
0
5
10
15
20
25
-10
-5
0
5
10

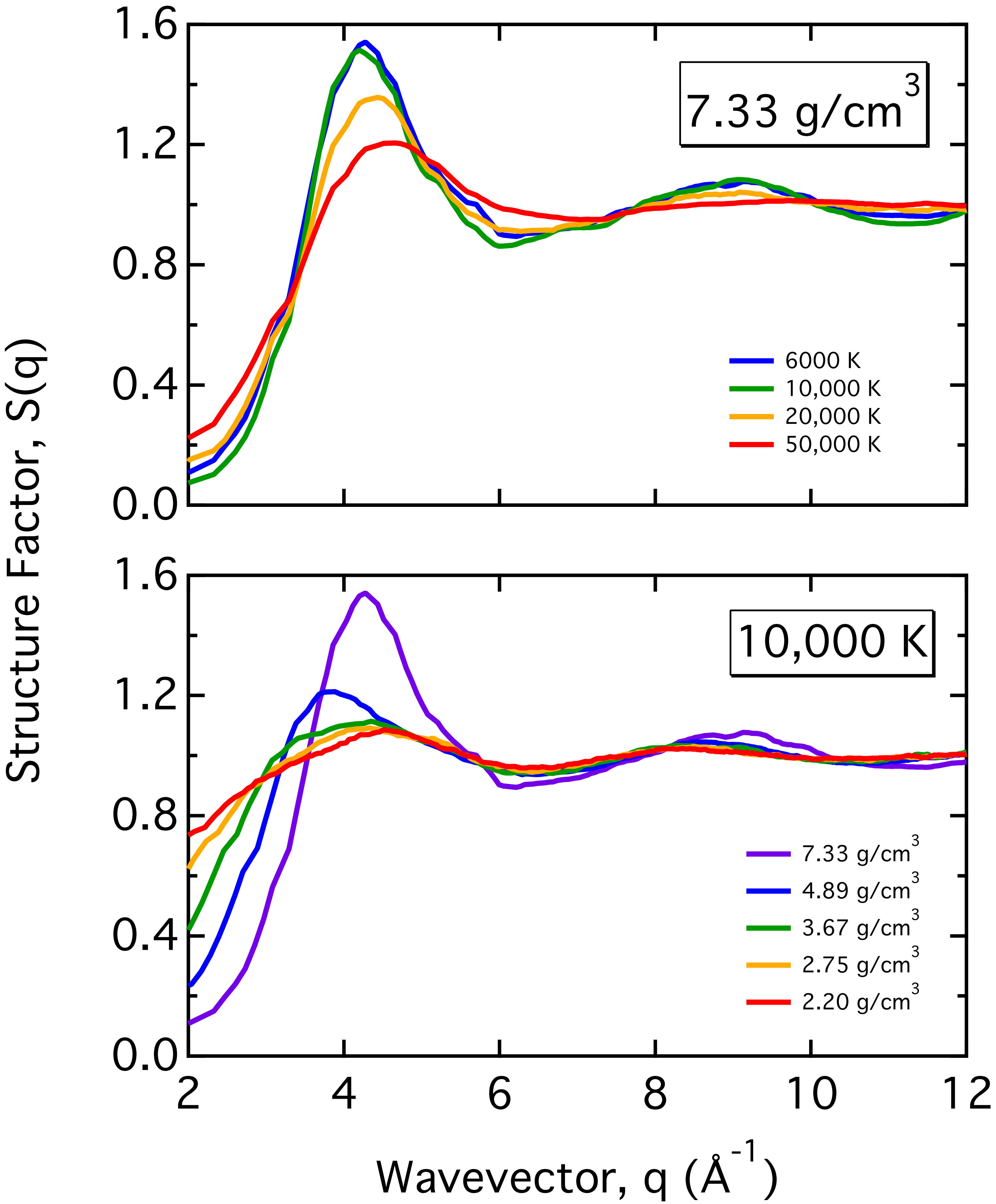
7.33 g/cm^3
6000 K
10,000 K
20,000 K
50,000 K
10,000 K
7.33 g/cm^3
4.89 g/cm^3
3.67 g/cm^3
2.75 g/cm^3
2.20 g/cm^3
Structure Factor, S(q)
Wavevector, q (Å^{-1})
0.0
0.4
0.8
1.2
1.6
2
4
6
8
10
12

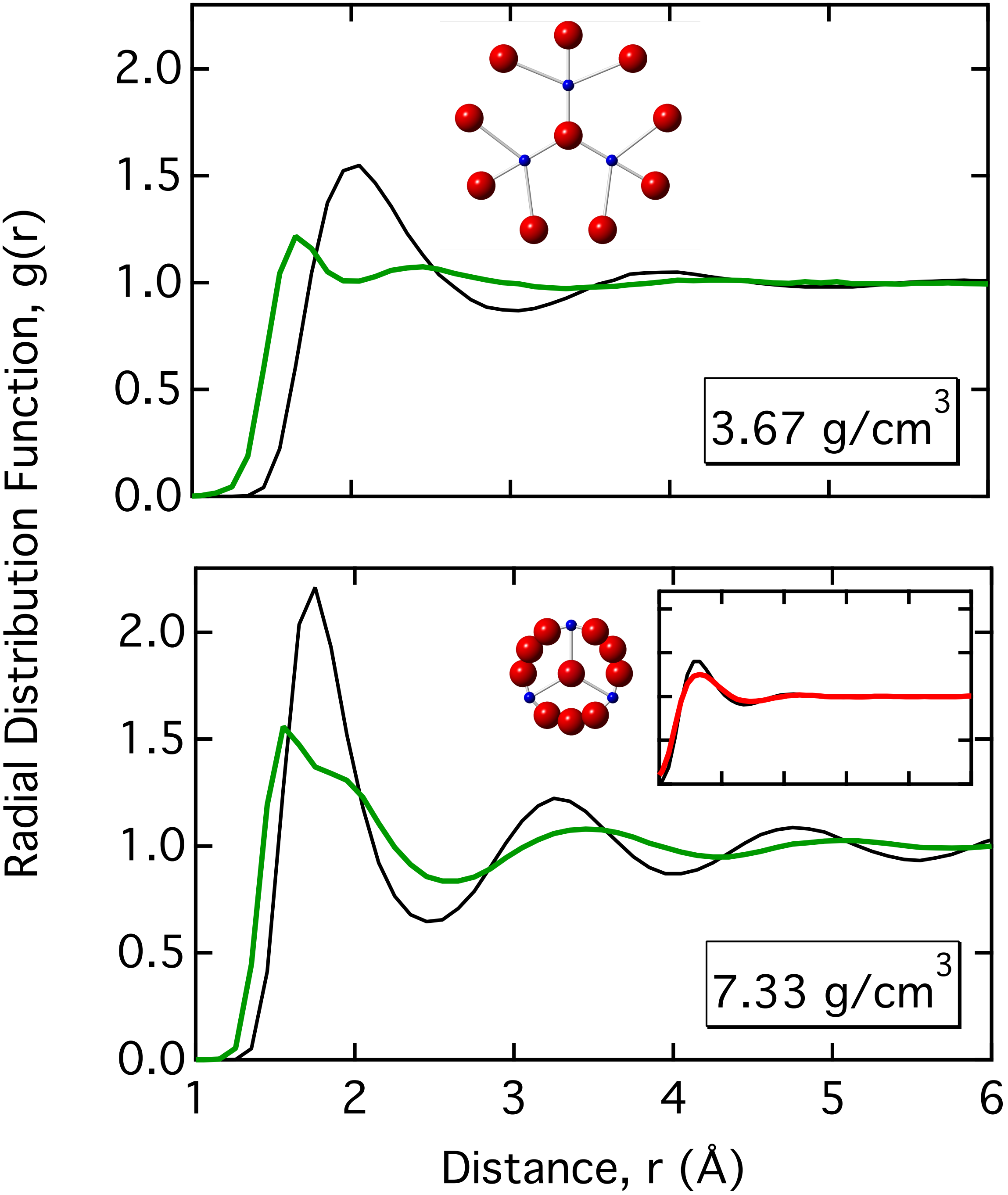
Radial Distribution Function, g(r)
2.0
1.5
1.0
0.5
0.0
3.67 g/cm^3
2.0
1.5
1.0
0.5
0.0
7.33 g/cm^3
1
2
3
4
5
6
Distance, r (Å)

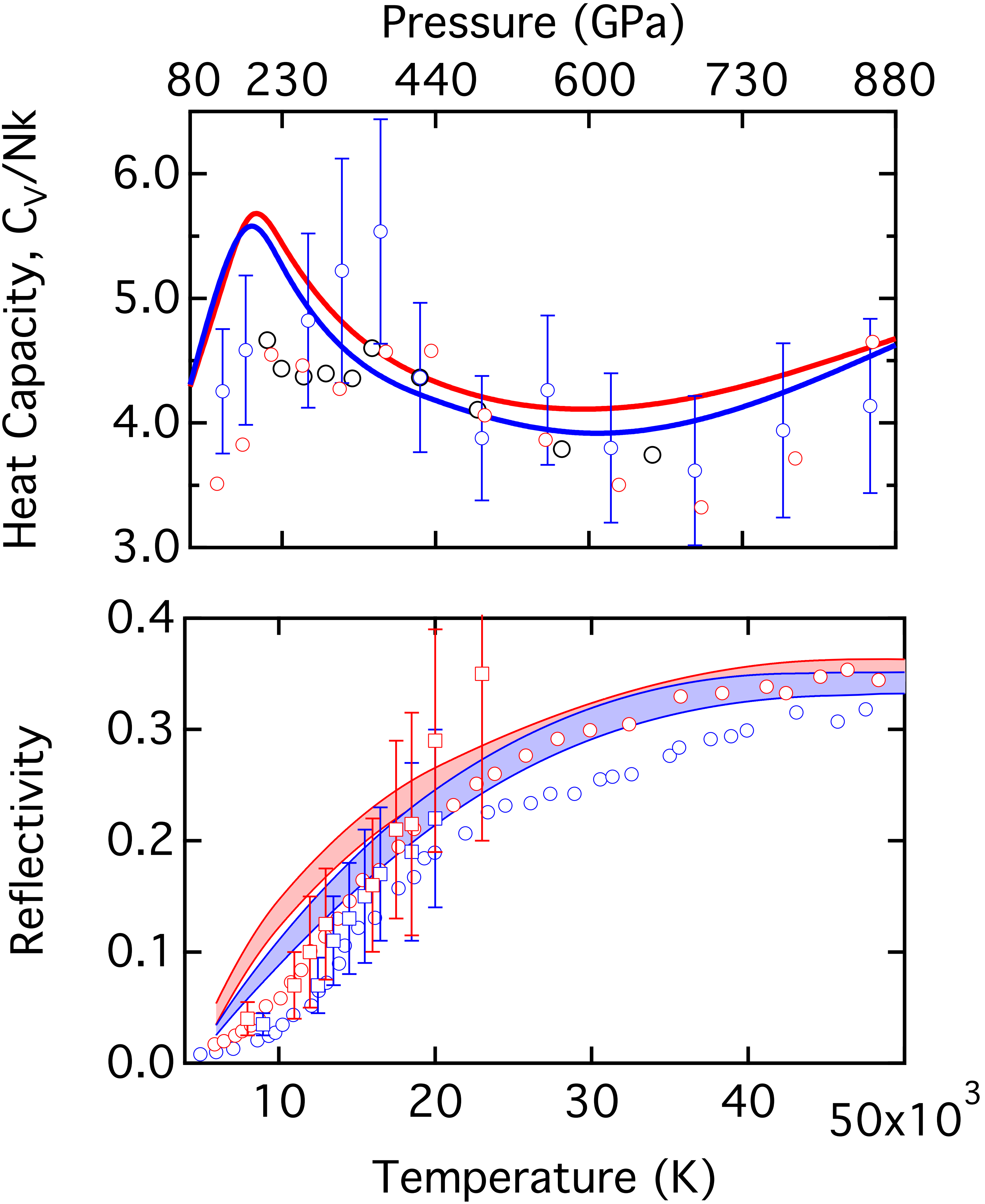
Pressure (GPa)
80
230
440
600
730
880
Heat Capacity, C_V/Nk
6.0
5.0
4.0
3.0
Reflectivity
0.4
0.3
0.2
0.1
0.0
10
20
30
40
50x10^3
Temperature (K)

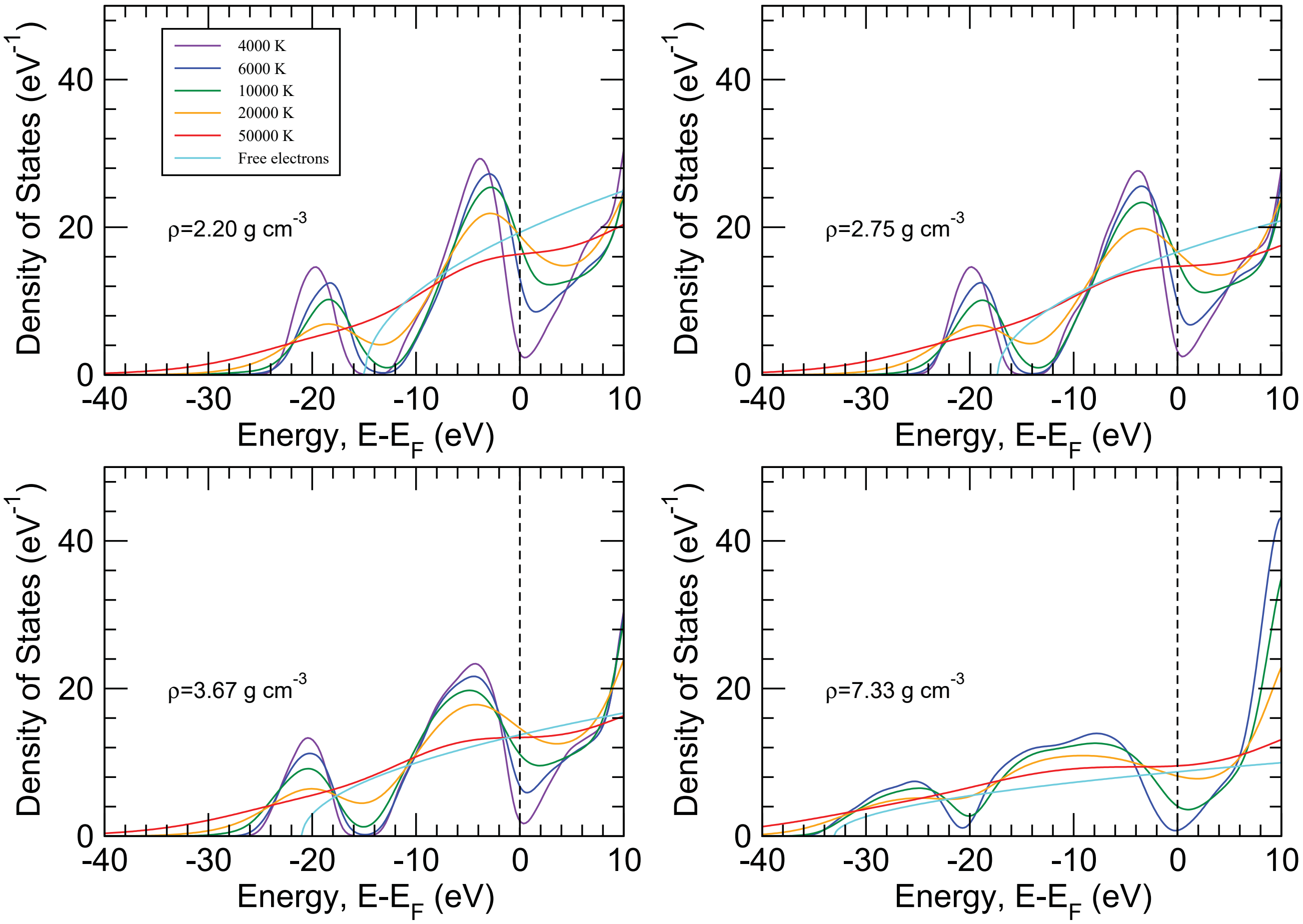
4000 K
6000 K
10000 K
20000 K
50000 K
Free electrons
ρ=2.20 g cm-3
ρ=2.75 g cm-3
ρ=3.67 g cm-3
ρ=7.33 g cm-3
Density of States (eV-1)
Energy, E-EF (eV)
0
20
40
-40
-30
-20
-10
0
10

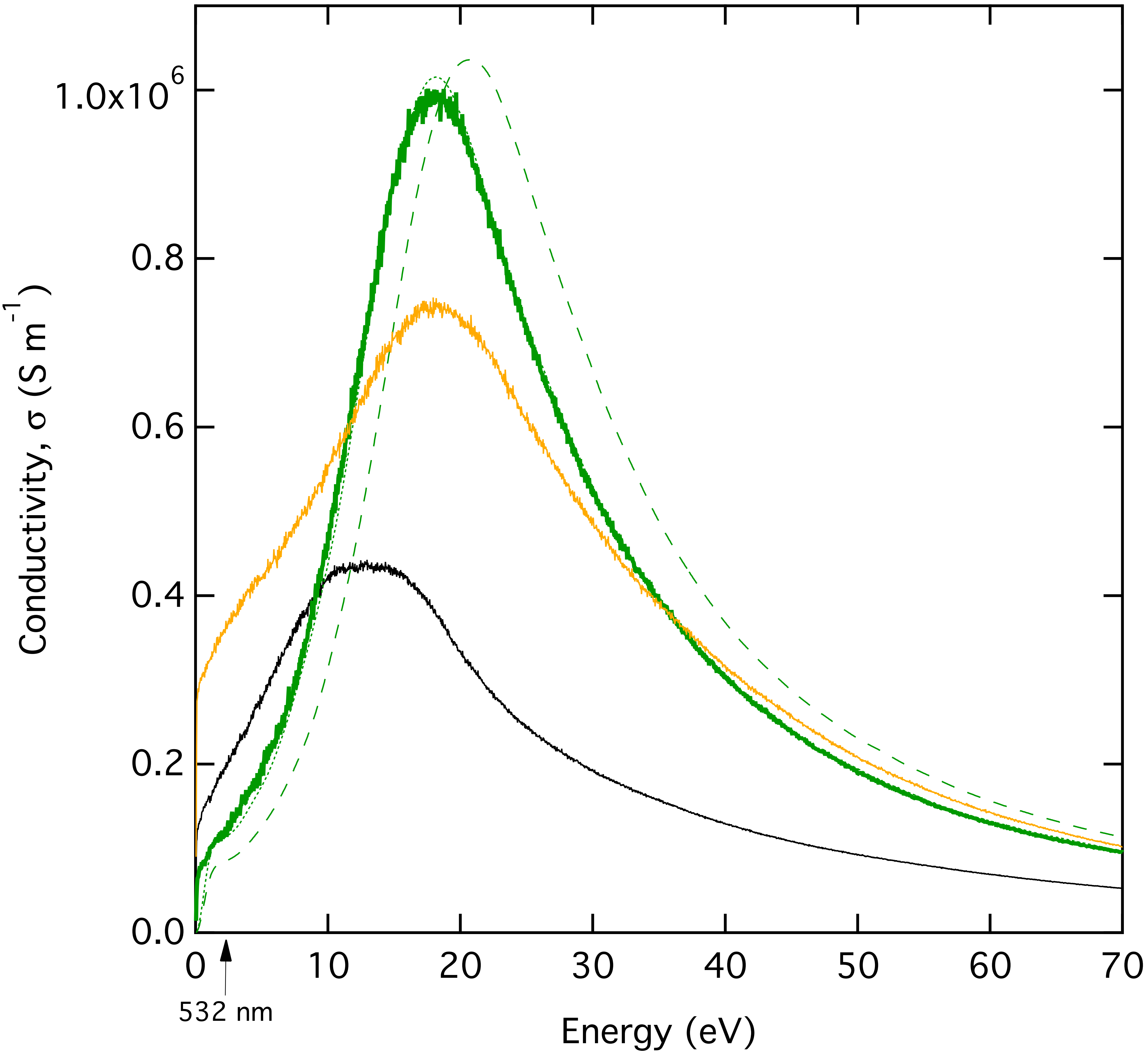
1.0x10^6
0.8
0.6
0.4
0.2
0.0
Conductivity, σ (S m^{-1})
0
10
20
30
40
50
60
70
Energy (eV)
532 nm

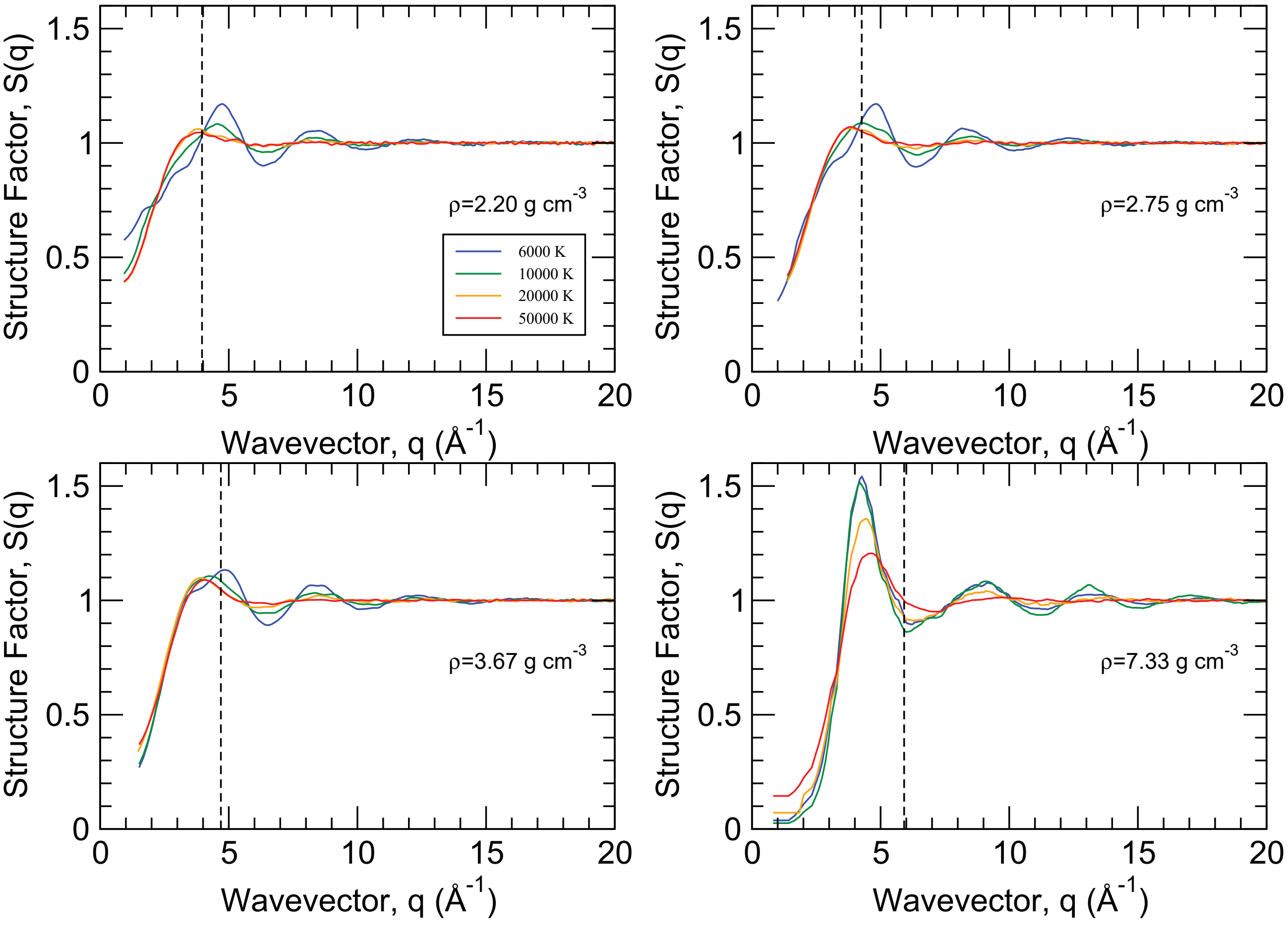
Structure Factor, S(q)
Wavevector, q (Å^{-1})
0
5
10
15
20
0
0.5
1
1.5
ρ=2.20 g cm^{-3}
6000 K
10000 K
20000 K
50000 K
ρ=2.75 g cm^{-3}
ρ=3.67 g cm^{-3}
ρ=7.33 g cm^{-3}

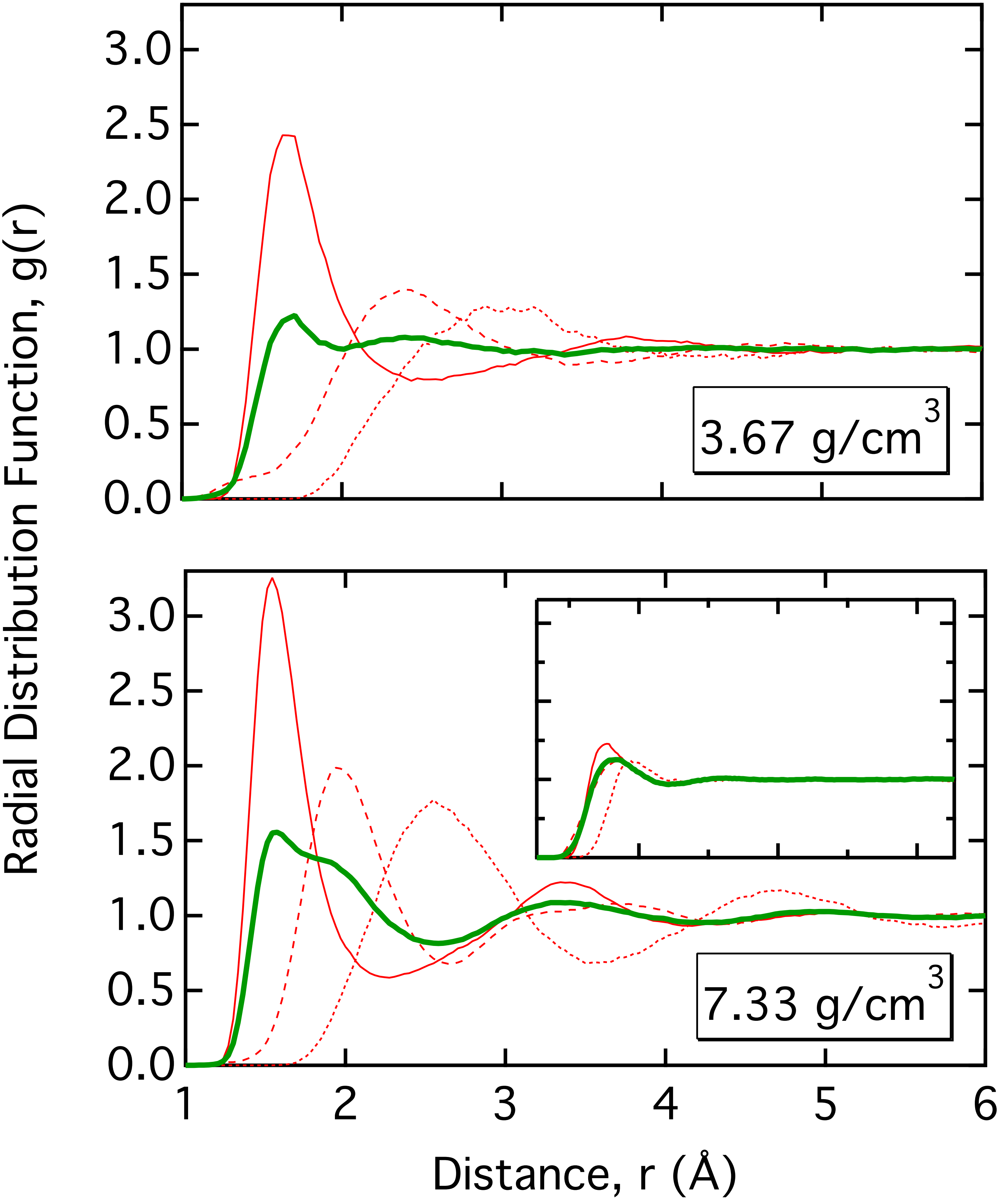
Radial Distribution Function, g(r)
3.0
2.5
2.0
1.5
1.0
0.5
0.0
3.67 g/cm^3
7.33 g/cm^3
1
2
3
4
5
6
Distance, r (Å)

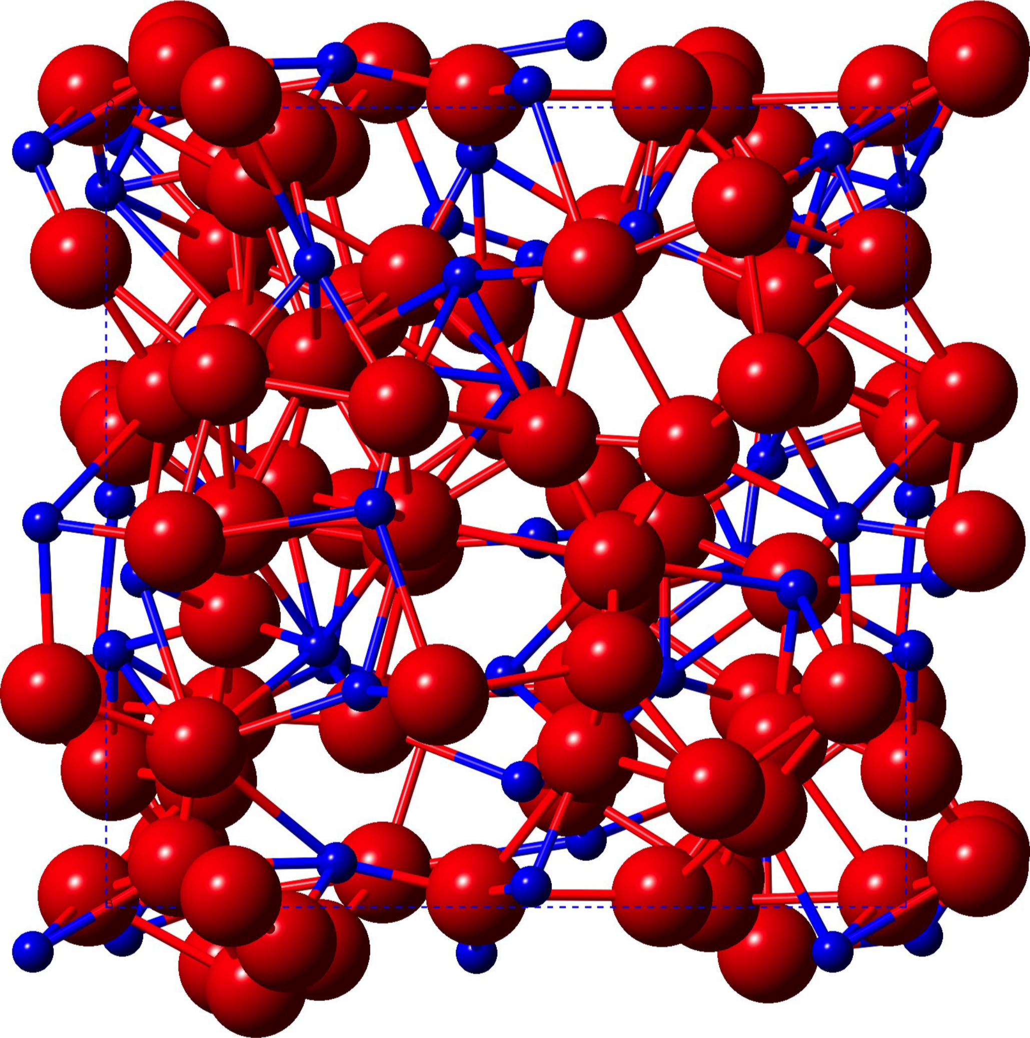
O
A
B

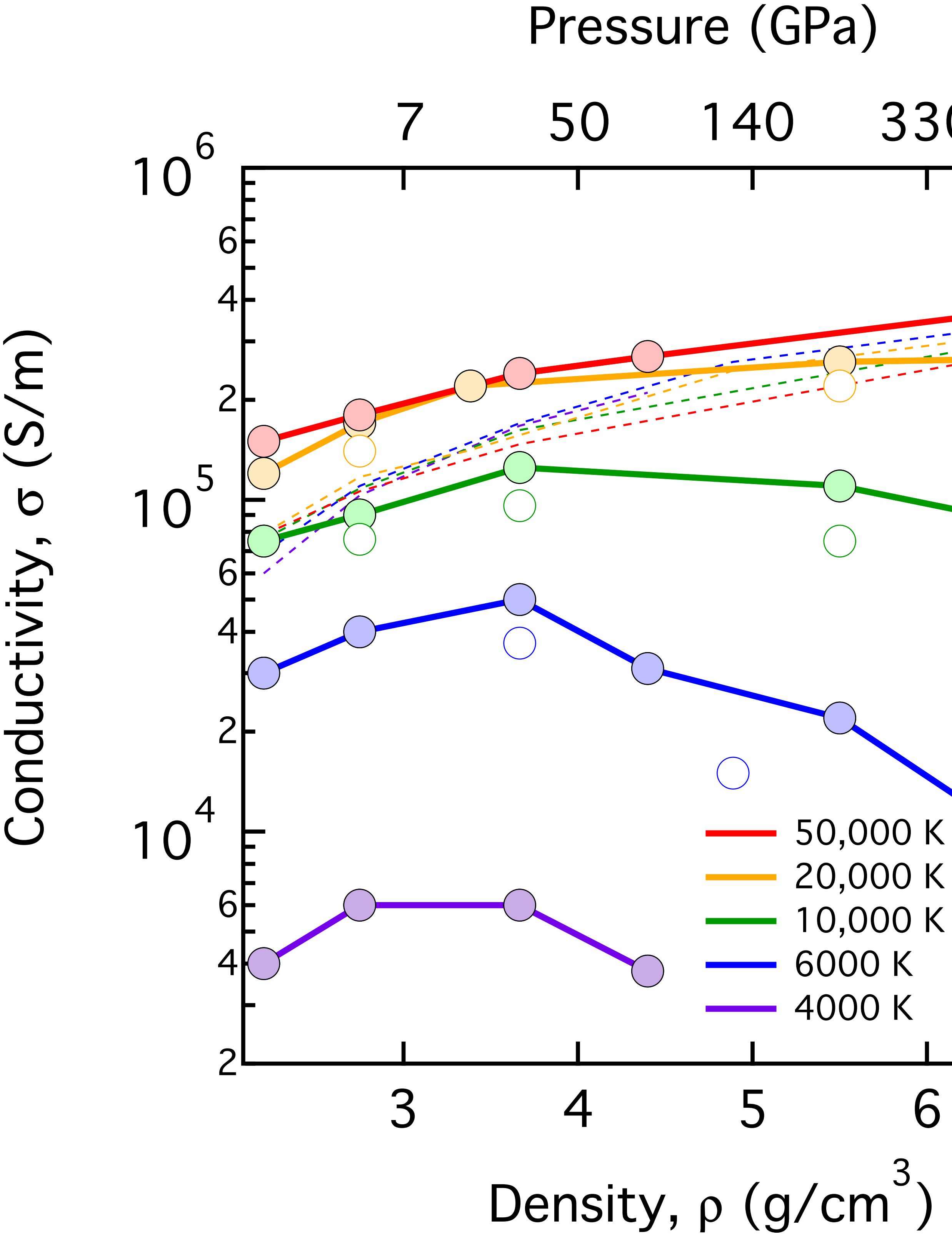
Pressure (GPa)
7
50
140
330
740
10^6
6
4
2
10^5
6
4
2
10^4
6
4
2
Conductivity, σ (S/m)
50,000 K
20,000 K
10,000 K
6000 K
4000 K
3
4
5
6
7
Density, ρ (g/cm^3)

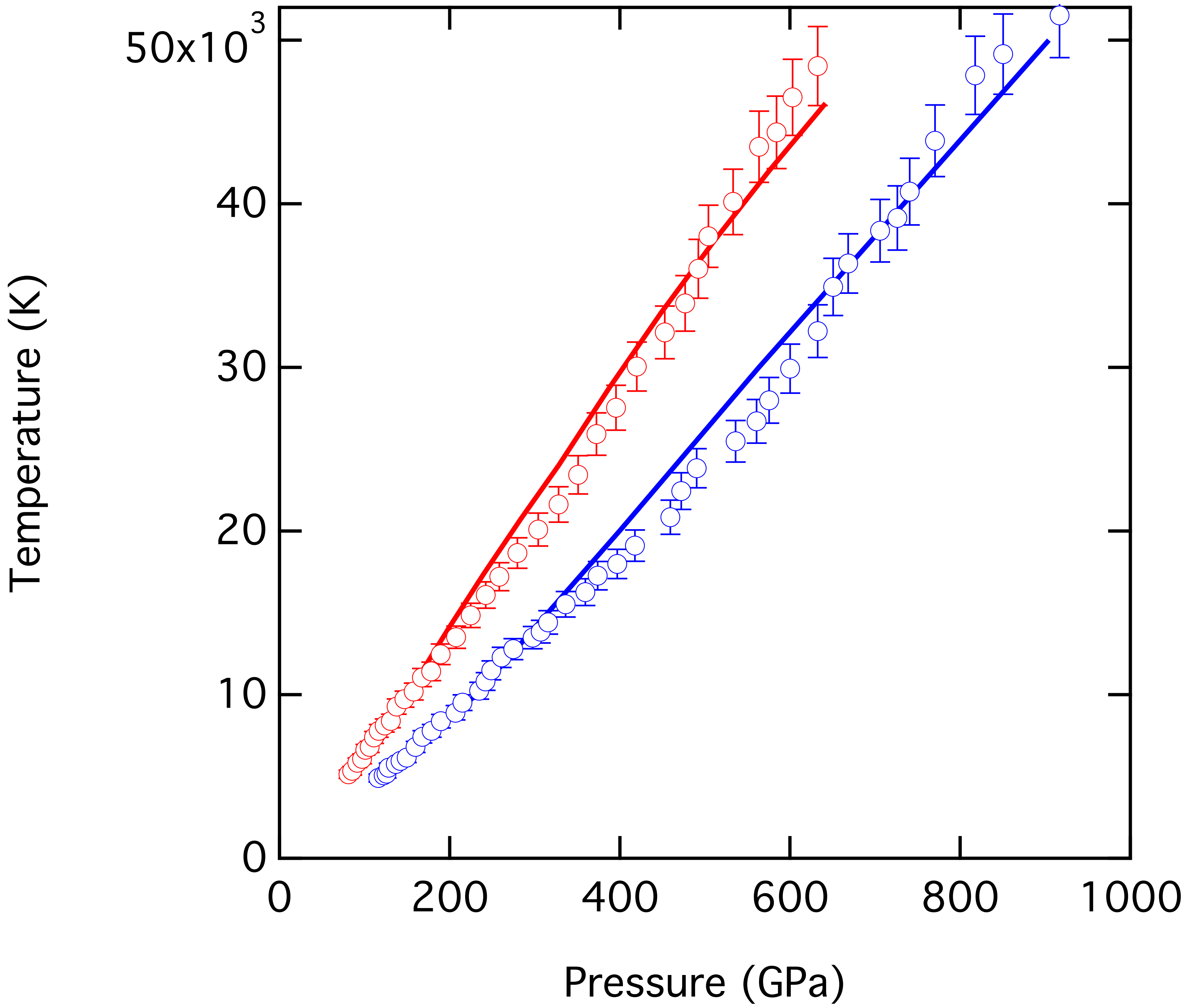

50x10^3
40
30
20
10
0
Temperature (K)
0
200
400
600
800
1000
Pressure (GPa)

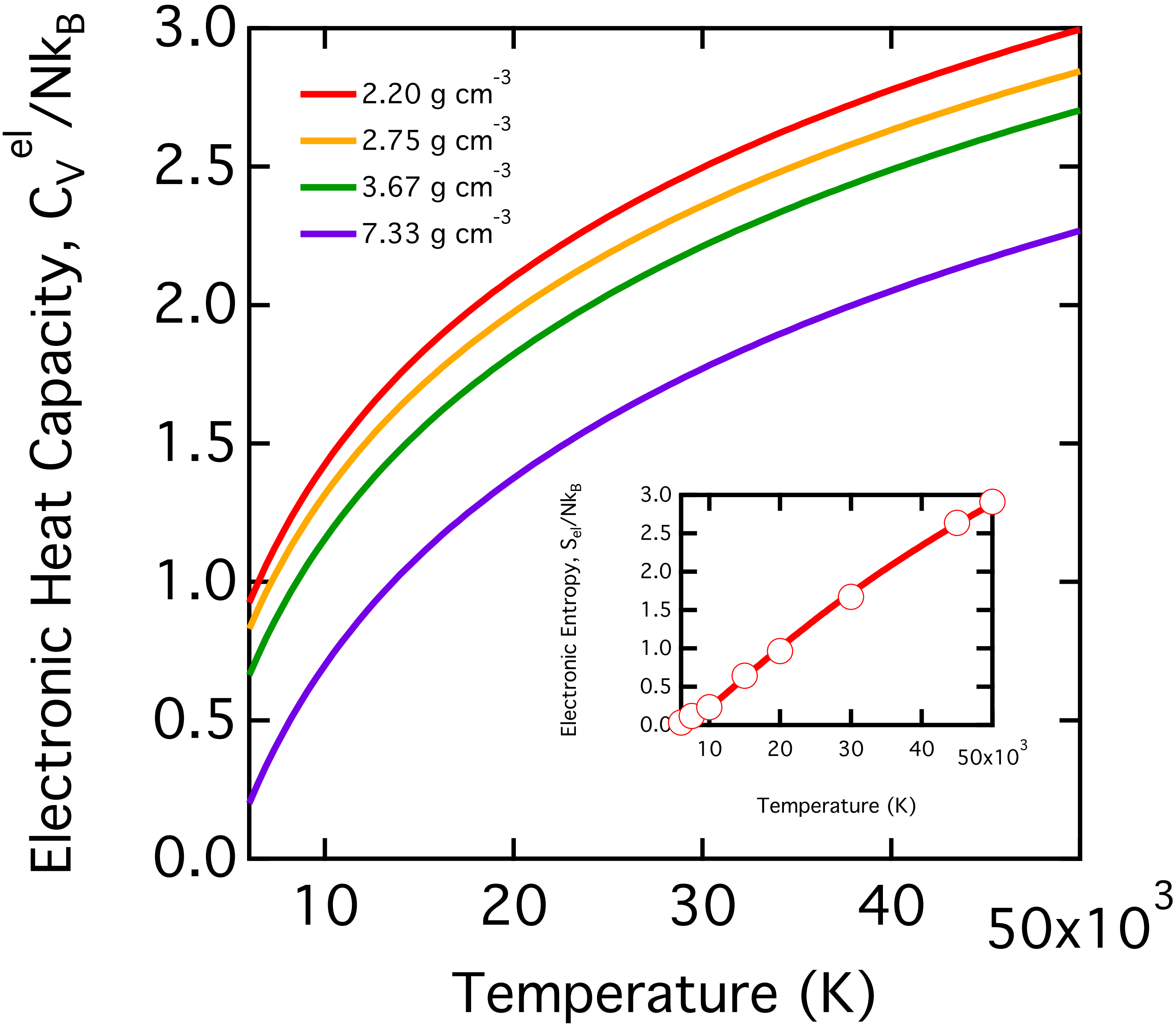
Electronic Heat Capacity, C_V^{el}/Nk_B
3.0
2.5
2.0
1.5
1.0
0.5
0.0
10
20
30
40
50x10^3
Temperature (K)
2.20 g cm^{-3}
2.75 g cm^{-3}
3.67 g cm^{-3}
7.33 g cm^{-3}
Electronic Entropy, S_{el}/Nk_B
3.0
2.5
2.0
1.5
1.0
0.5
0.0
10
20
30
40
50x10^3
Temperature (K)

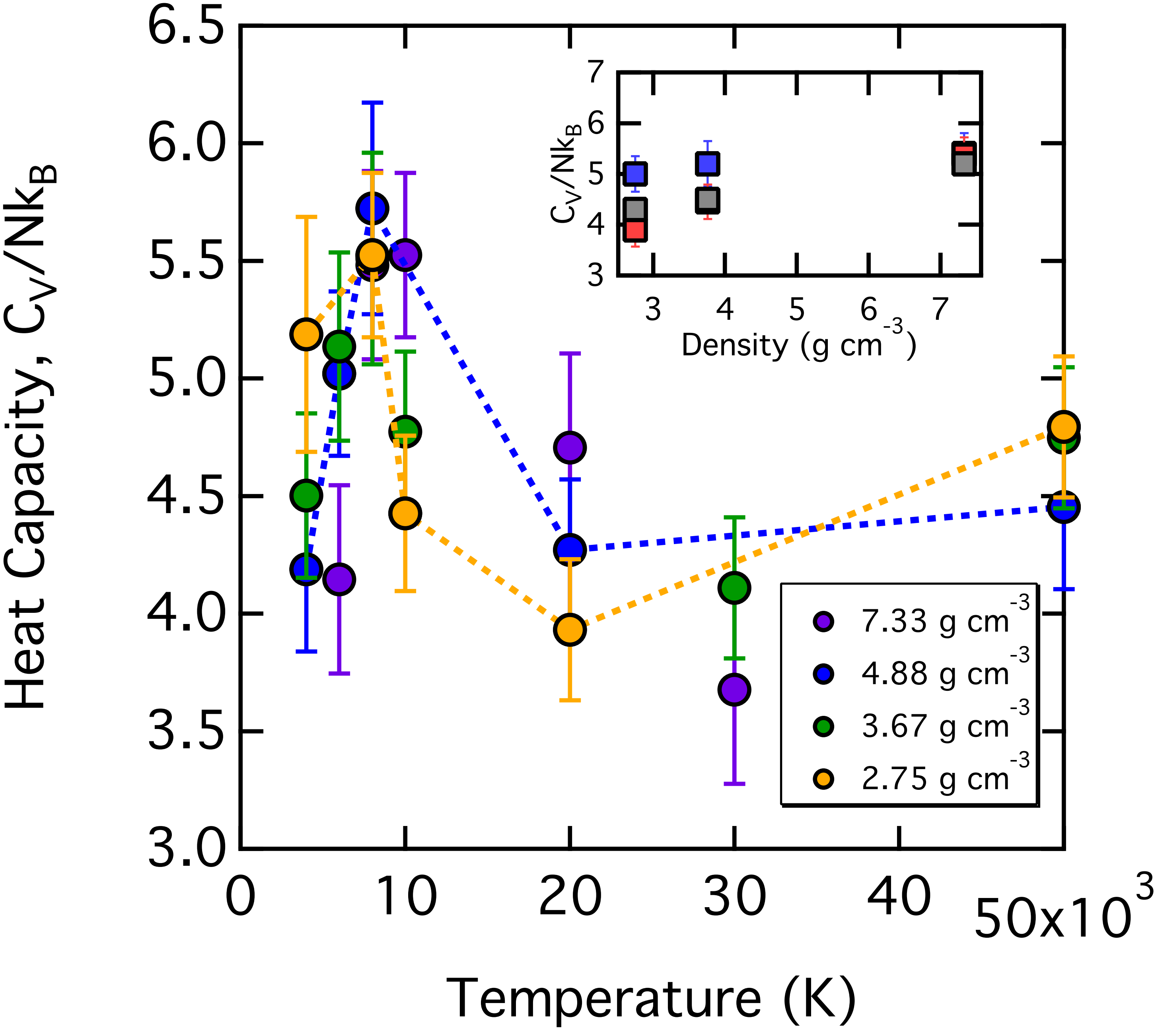
Heat Capacity, C_V/Nk_B
6.5
6.0
5.5
5.0
4.5
4.0
3.5
3.0
0
10
20
30
40
50×10^3
Temperature (K)
7.33 g cm^{-3}
4.88 g cm^{-3}
3.67 g cm^{-3}
2.75 g cm^{-3}
C_V/Nk_B
7
6
5
4
3
3
4
5
6
7
Density (g cm^{-3})